Proceedings 10th NUMGE 2023

10th European Conference on Numerical Methods in Geotechnical Engineering Zdravkovic L, Kontoe S, Taborda DMG, Tsiampousi A (eds)

© Authors: All rights reserved, 2023 https://doi.org/10.53243/NUMGE2023-395

Micro-polar periporomechanics for shear bands and cracks in porous media under dynamic loads

X. Song¹, H. Pashazad¹

¹Department of Civil and Coastal Engineering, University of Florida, Gainesville, Florida, USA

ABSTRACT: Periporomechanics is a strong nonlocal framework for modeling the mechanics and physics of variably saturated porous media with evolving discontinuities. In this article, as a new contribution we formulate a Cosserat periporomechanics paradigm for modeling dynamic shear banding and crack branching in porous media incorporating a micro-structure based length scale. In this micro-periporomechanics framework, each material point has translational and rotational degrees of freedom following the Cosserat continuum. A stabilized Cosserat constitutive correspondence principle is used to incorporate classical viscous elastic and plastic material models for porous media in the proposed Cosserat periporomechanics. We have numerically implemented the micro-periporomechanics paradigm through an explicit algorithm in time and a Lagrangian meshfree method in space. Numerical examples are presented to demonstrate the efficacy and robustness of the micro-periporomechanics for modeling shear banding and crack branching in single-phase porous media under dynamic loads.

Keywords: Micro-polar model; Periporomechanics; Dynamic failure; Porous media; Crack branching

1 INTRODUCTION

Periporomechanmics is a strong nonlocal framework for modeling the mechanics and physics of variably saturated porous media with evolving discontinuities (Song and Silling, 2020, Menon and Song, 2021a and b). In periporomechanics, it is postulated that material points within a finite distance called the horizon have direct mechanical and physical interactions. The horizon plays the role of a spatial length scale in the framework. However, it lacks a clear physical meaning. In this article, as a new contribution, we formulate a Cosserat periporomechanics paradigm in which a micro-polar length scale is incorporated through the Cosserat continuum (Sulem and Vardoulakis, 1995).

The micro-polar periporomechanics paradigm formulated in this study is based on the total Lagrangian formulation. The updated Lagrangian formulation of periporomechanics for large deformation with and without discontinuities (e.g., cracks) can be found in the literature (e.g., Menon and Song, 2022b, Menon and Song, 2023). In this micro-polar periporomechanics paradigm, each material point has both translational and rotational degrees of freedom following the Cosserat continuum. The governing equations consist of the balance equations of the linear momentum and moment. For modeling fracture propagation, the energy-based crack criterion through the effective force state concept for unsaturated porous media (Menon and Song, 2022a) was reformulated by considering both the displacement and rotation degrees of freedom.

In the proposed Cosserat periporomechanics, a stabilized Cosserat constitutive correspondence principle is used to incorporate classical viscous elastic and plastic material models for porous media. We refer to the literature for the non-polar multiphase constitutive correspondence principle and its stabilization (Song and Silling, 2020, Menon and Song, 2021a and b). A micropolar viscoplastic constitutive model for the solid skeleton is implemented to simulate the time-dependent behavior of geomaterials. An energy-based damage model is utilized to model the bond breakage. In this study, the meshless method in space and an explicit Newmark scheme in time are used to solve the governing equations. Two numerical examples are presented to demonstrate the robustness and efficacy of the proposed Cosserat periporomechanics paradigm for modeling shear bands and crack branching in dry porous media. Example 1 deals with shear banding under high loading rates and the effect of material parameters on the shear band formation. Example 2 deals with the crack branching under high loading rates.

2 MATHEMATICAL FORMULATION

This section presents the governing equations of the micro-polar periporomechanics paradigm for porous media under dry conditions (e.g., single phase), which consist of the balance equations of force and moment. For notation, the variable with no prime is associated with the material point \boldsymbol{x} and the variable with a prime is

associated with the material point x' (Menon and Song, 2021a, b). First, the force balance equation is written as

$$\rho^{s} \ddot{\boldsymbol{u}} = \int_{\mathcal{H}} \left(\underline{\overline{T}} - \underline{\overline{T}}' \right) dV' + \rho^{s} \boldsymbol{g}$$
 (1)

where \mathcal{H} is a neighborhood of material point \mathbf{x} , and $\ddot{\mathbf{u}}$ is the acceleration, \mathbf{g} is gravitational acceleration, ρ^s is the partial density of the solid skeleton, and $\overline{\mathbf{T}}$ is the effective force state. The partial density of solid ρ^s (Song and Borja, 2014, and Song et al., 2017) is written as

$$\rho^{s} = \phi^{s} \rho_{s} \tag{2}$$

where ρ_s is the intrinsic density of the solid skeleton and ϕ^s is the volume fraction of the solid. Assuming an incompressible solid phase, ϕ^s can be written as

$$\phi^s = \frac{\phi_0^s}{I} \tag{3}$$

where $J = det(\overline{F})$, ϕ_0^s is the initial volume fraction, and \overline{F} is the nonlocal approximate deformation gradient (Silling et al., 2007). \overline{F} is defined as

$$\overline{\mathbf{F}} = \left[\int_{\mathcal{H}} \underline{\omega} \left(\underline{\mathbf{Y}} \otimes \boldsymbol{\xi} \right) dV' \right] \overline{\mathbf{K}}^{-1} \tag{4}$$

where $\underline{\omega}$ is the influence function, \overline{K}^{-1} is the shape tensor, \underline{Y} is the deformation vector state, $\xi = x' - x$, and x' and x are the spatial locations of two material points in the initial configuration (Song and Silling, 2020). Second, the moment balance equation for the micro-polar periporomechanics is written as

$$I^{s} \ddot{\boldsymbol{\omega}} = \int_{\mathcal{H}} \left(\underline{\boldsymbol{M}} - \underline{\boldsymbol{M}}' \right) dV' + \frac{1}{2} \int_{\mathcal{H}} \underline{\boldsymbol{Y}} \times \left(\overline{\underline{\boldsymbol{T}}} - \underline{\boldsymbol{T}}' \right) dV' + \boldsymbol{l}$$
 (5)

where \boldsymbol{l} and \boldsymbol{l}^s denote body couple density and microinertia of solid, respectively, $\boldsymbol{\omega}$ is micro-rotation vector, $\ddot{\boldsymbol{\omega}}$ is angular acceleration, and $\underline{\boldsymbol{M}}$ is the moment state.

For geomaterials, I^s is the momentum of inertia for the solid skeleton. By considering the mean grain size in porous media as the micro-polar length scale l, the moment of inertia (Sulem and Vardoulakis, 1995) can be written as

$$I^{s} = \frac{1}{2}\pi\phi^{s}\rho_{s} l^{2} \tag{6}$$

2.1 Constitutive correspondence principle

In this study, the periporomechanics constitutive correspondence principle (Menon and Song 2021a) is augmented to determine the effective force state and moment state from the effective stress and couple stress as

$$\overline{T} = \omega \sigma \overline{K}^{-1} \xi \tag{7}$$

$$\underline{M} = \underline{\omega} m \overline{K}^{-1} \xi \tag{8}$$

where σ is the stress and m is the couple stress, which are energy conjugates to the strain tensor ε and wryness tensor κ . The non-local approximations to the strain tensor ε and wryness tensor κ can be written as

$$\boldsymbol{\varepsilon} = \left[\int_{\mathcal{H}} \underline{\omega} \left(\underline{\boldsymbol{U}}_{\underline{\tilde{\boldsymbol{\Omega}}}} \otimes \boldsymbol{\xi} \right) dV' \right] \overline{\boldsymbol{K}}^{-1} \tag{9}$$

$$\boldsymbol{\kappa} = \left[\int_{\mathcal{H}} \underline{\omega} \left(\underline{\Omega} \otimes \boldsymbol{\xi} \right) dV' \right] \overline{\boldsymbol{K}}^{-1}$$
 (10)

where $\underline{U}_{\underline{n}}$ and \underline{n} are composite and relative rotation states, which are written as

$$\underline{\underline{U}_{\underline{\tilde{\alpha}}}} = (\underline{u}' - \underline{u}) + \frac{1}{2}(\underline{\omega}' + \underline{\omega}) \times (\underline{x}' - \underline{x})$$
(11)

$$\mathbf{\Omega} = \mathbf{\omega}' - \mathbf{\omega} \tag{12}$$

2.2 Micro-polar constitutive models

In this part, we first introduce the classical micro-pola visco-plasticity model cast in the classical Cosserat continuum framework. Then, we present a micro-polar damage model with an energy criterion incorporating translational and micro-rotation deformation energy.

2.2.1 Micro-polar viscoplastic constitutive model

The strain tensor ε and the wryness tensor κ are additively decomposed into elastic and viscoplastic parts as

$$\varepsilon = \varepsilon^e + \varepsilon^{vp} \tag{13}$$

$$\kappa = \kappa^e + \kappa^{vp} \tag{14}$$

where $\boldsymbol{\varepsilon}^{e}$ and $\boldsymbol{\varepsilon}^{vp}$ are the elastic and viscoplastic strain tensors, respectively, and $\boldsymbol{\kappa}^{e}$ and $\boldsymbol{\kappa}^{vp}$ are the elastic and viscoplastic wryness tensors, respectively. The stress $\boldsymbol{\sigma}$ and the couple stress \boldsymbol{m} are written as

$$\boldsymbol{\sigma} = \lambda tr(\boldsymbol{\varepsilon}^e) 1 + (\mu + \mu_c) \boldsymbol{\varepsilon}^e + (\mu - \mu_c) \boldsymbol{\varepsilon}^{e^T}$$
(15)

 $\boldsymbol{m} = \alpha_1 tr(\boldsymbol{\kappa}^e) 1 + \alpha_2 \boldsymbol{\kappa}^e + \alpha_3 \boldsymbol{\kappa}^{e^T}$ (16) where λ , μ , μ_c , α_1 , α_2 and α_3 are material parameters. In three dimensions, the stress and the couple stress can be written in a vector form as

$$\widetilde{\sigma} = {\{\sigma_{11}, \sigma_{22}, \sigma_{33}, \sigma_{12}, \sigma_{21}, \sigma_{13}, \sigma_{31}, \sigma_{23}, \sigma_{32}\}^T}$$
(17)

$$\widetilde{m} = \{m_{11}/l, m_{22}/l, m_{33}/l, m_{12}/l, m_{21}/l, m_{13}/l, m_{31}/l, m_{23}/l, m_{32}/l\}^T$$
 (18)

In this study, we adopt the generalized Drucker-Prager yield function which is written as

$$\mathbf{f} = q + \sqrt{3}A_{\phi}p + B \tag{19}$$

where q is the deviatoric stress and p is the effective mean stress, which are defined as

$$q = \sqrt{\frac{1}{2} \left(\widetilde{\boldsymbol{\sigma}}^T \widetilde{\mathbb{P}} \ \widetilde{\boldsymbol{\sigma}} + \widetilde{\boldsymbol{m}}^T \widetilde{\widetilde{\mathbb{P}}} \ \widetilde{\boldsymbol{m}} \right)}$$
 (20)

$$p = \frac{\widetilde{\sigma_1} + \widetilde{\sigma_2} + \widetilde{\sigma_3}}{3} \tag{21}$$

In (20)

$$\widetilde{\mathbb{P}} = \begin{bmatrix} \widetilde{\mathbb{P}}^I & 0 \\ 0 & \widetilde{\mathbb{P}}^{II} \end{bmatrix} \tag{22}$$

$$\widetilde{\mathbb{P}}^{I} = \begin{bmatrix} 2 & -1 & -1 \\ -1 & 2 & -1 \\ -1 & -1 & 2 \end{bmatrix}$$
 (23)

$$\widetilde{\mathbb{P}}^{II} = \begin{bmatrix} 3/2 & 3/2 \\ 3/2 & 3/2 \\ & & 3/2 & 3/2 \\ & & & 3/2 & 3/2 & 3/2 \\ & & & & 3/2 & 3/2 & 3/2 \end{bmatrix} (24)$$

and

$$\widetilde{\mathbb{P}} = 3I_{9\times9} \tag{25}$$

The variables A_{Φ} and B in (19) are defined as

$$A_{\phi} = \frac{2\sin\phi}{\sqrt{3}(3-\sin\phi)} \tag{26}$$

$$B = \frac{-6c\cos\phi}{\sqrt{3}(3-\cos\phi)} \tag{27}$$

where ϕ is the frictional angle and c is the cohesion. In this study, a linear hardening law is adopted, which is defined as

$$c = c_0 + h\overline{\epsilon} \tag{28}$$

where h is the linear hardening modulus and $\overline{\epsilon}$ is the internal hardening variable. For the non-associative plasticity, the plastic potential is written as

$$g = q + \sqrt{3}A_{\psi}p + B \tag{29}$$

$$A_{\psi} = \frac{2\sin\psi}{\sqrt{3}(3-\sin\psi)} \tag{30}$$

where ψ is the dilatancy angle. The viscoplastic strain and wryness tensors can be defined as

$$\boldsymbol{\varepsilon}^{\boldsymbol{v}\boldsymbol{p}} = \frac{\langle f \rangle}{\eta'} \frac{\partial g}{\partial \sigma} \tag{31}$$

$$\kappa^{vp} = \frac{\langle f \rangle}{n} \frac{\partial g}{\partial m} \tag{32}$$

where η' is the viscosity and the angle bracket is the Macaulay bracket. The plastic internal variable is defined as

$$\bar{\varepsilon} = \frac{\langle f \rangle}{\eta'} (1 + sign(p) \frac{A_{\psi}}{\sqrt{3}})$$
 (33)

2.2.2 Damage model

For the Cosserat periporomechanics paradigm, the bond breakage between material points is modeled through an energy criterion that accounts for translational displacement and micro-rotation. The effective force state and the moment state, which are the energy conjugates to the composite state and the relative rotation state, are used to determine the deformation energy. In this case, the energy density in the bond ξ reads

$$w_{\xi} = \int_{0}^{t} (\overline{\underline{T}} - \overline{\underline{T}}') \dot{\boldsymbol{\eta}} dt + \int_{0}^{t} (\underline{\boldsymbol{M}} - \underline{\boldsymbol{M}}') \dot{\boldsymbol{\theta}} dt$$
(34)

where $\eta = (u' - u) + 0.5(\omega' + \omega) \times (x' - x)$ and $\theta = \omega' - \omega$ and t is the total loading time. The bond breakage is tracked through the influence function at material points. The influence function is written as

$$\underline{\omega} = \begin{cases} 1 & \text{if } w_{\xi} < w_{cr} \\ 0 & \text{if } w_{\xi} \ge w_{cr} \end{cases}$$
 (35)

where w_{cr} is the critical bond energy. The bond-breakage criterion depends on the deformation energy stored in a bond. Based on this criterion, the energy density stored in a bond, w_{ξ} , is recoverable until it exceeds a critical value, w_{cr} . Finally, a local damage variable at each material point, which is used for tracking crack propagation, can be defined as

$$D = 1 - \frac{\int_{\mathcal{H}} \omega \, dv'}{\int_{\mathcal{H}} dv'} \tag{36}$$

2.3 Numerical implementation

We have implemented the proposed Cosserat periporomechanics paradigm through a Lagrangian meshfree method in space and an explicit Newmark scheme in time. In this method, a porous material body is discretized into a finite number of uniform material points. Each material point is endowed with two types of degrees of freedom, i.e., translational displacement and micro-rotation. The boundary conditions are applied to the boundary layers (Menon and Song, 2022b). For more details on the numerical implementation, we refer to the literature (Menon and Song, 2022b and 2023).

3 NUMERICAL EXAMPLES

3.1 Dynamic shear banding

This example deals with dynamic shear banding. Figure 1 plots the model set up for this example. The specimen's length, width, and thickness are 200 mm, 100 mm, and 10 mm, respectively. A vertical displacement of $u_y = 4.5$ mm is applied on the top and bottom boundaries with a rate of $\dot{u}_y = 0.05$ m/s. The constant lateral confining pressure of $\sigma_0 = 0.1$ MPa is applied on the left and right boundaries. The material parameters adopted are density $\rho^s = 2000 \text{ kg/m}^3$, $\lambda = 13.9 \text{ MPa}$, $\mu = 20.8 \text{ MPa}, \mu_c = 2\mu, \alpha_3 = 83.3 \text{ kN}, \alpha_1 = \alpha_2 = 0,$ initial volume fraction $\phi_0^s = 0.65$, the micro-polar length scale l=2 mm, $c_0=0.35$ MPa, h=-1 MPa, and $\eta=$ 0.01 MPa.s. The specimen is discretized into 40×80 material points with a uniform grid $\Delta x = 2.5$ mm and the horizon $\delta = 2.05 \Delta x$. The total simulation time t = $0.1 \text{ s with } \Delta t = 7 \text{ µs.}$

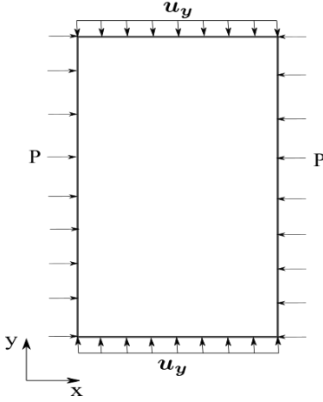


Figure 1. Schematic of the model setup for example 1

We present the results from the simulations assuming three frictional angles, i.e., $\phi=25^{\circ},35^{\circ}$, and 45°, and the same dilatation angle $\psi=15^{\circ}$. Figure 2 plots the loading curves from the three simulations. The results in Figure 2 show that the friction angle affects the peak loads and the post-localization stage. Figure 3 plots the contours of the equivalent plastic shear strain superimposed on the deformed configurations for the

three simulations. The results show that the two conjugate shear bands have formed in the three simulations. The inclination anlge of shear bands are similar for the three simulations, although the friction angles are different. Figure 4 plots the contours of the micro-rotation on the deformed configuration. The results show that the micro rotation of material points is localized around the shear band, as shown in the experimental testing results (Sulem and Vardoulakis, 1995).

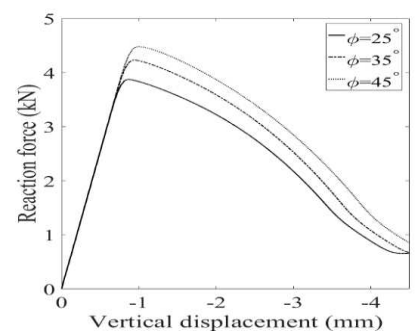


Figure 2. Loading curves from the simulations with $\phi = 25^{\circ}$, 35° and 45°

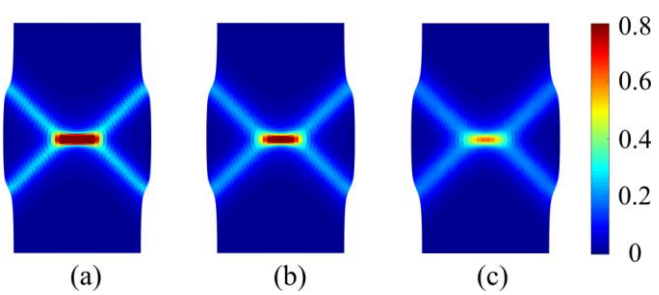


Figure 3. Contours of the equivalent plastic shear strain from the simulations: (a) $\phi_1 = 25^{\circ}$, (b) $\phi_2 = 35^{\circ}$, and (c) $\phi_3 = 45^{\circ}$

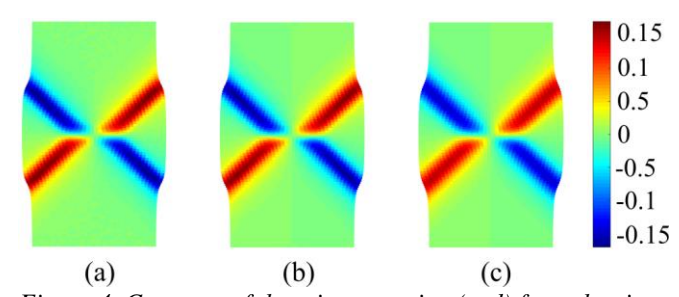


Figure 4. Contours of the micro rotation (rad) from the simulations: (a) $\phi_1=25^\circ$, (b) $\phi_2=35^\circ$, and (c) $\phi_3=45^\circ$

Next, we present the simulations with three dilatation angles, i.e., $\psi=0^{\circ},15^{\circ}$ and 30° , and $\phi=35^{\circ}$. Figure 5 plots the loading curves from the three simulations, which show that the dilatation angle only slightly affects loading curves. Figure 6 plots the contours of the equivalent plastic shear strain (the shear band angle shown in the bracket). The results show that the dilation angle affects the inclination angle of shear bands. Figure 7 plots the contours of micro rotations of material points. The results are consistent with the simulations assuming different friction angles, as shown in Figure 4.

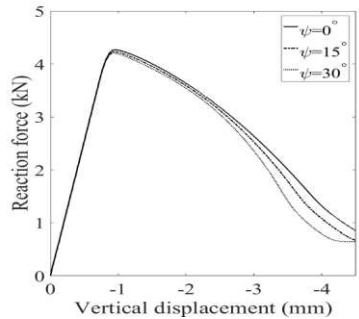


Figure 5. Loading curves from the simulations with $\psi = 0^{\circ}$, 15° and 30°, respectively

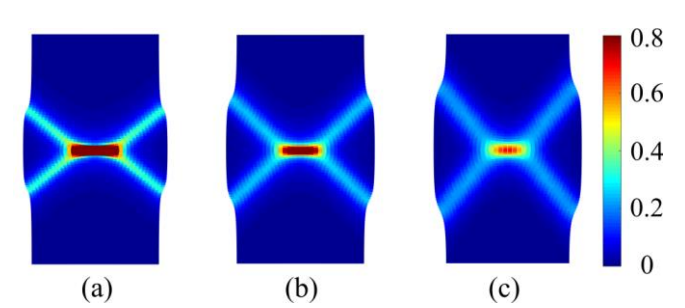


Figure 6. Contours of the equivalent plastic shear strain from the simulations: (a) $\psi_1=0^\circ(41.3^\circ)$, (b) $\psi_2=15^\circ~(48.9^\circ)$, and (c) $\psi_3=30^\circ(56.4^\circ)$.

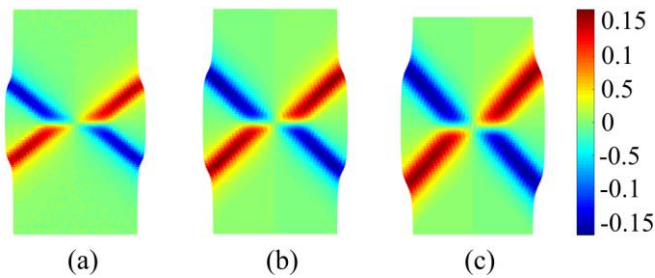


Figure 7. Contours of the micro rotation (rad) from the simulations: (a) $\psi_1 = 0^\circ$, (b) $\psi_2 = 15^\circ$, and (c) $\psi_3 = 30^\circ$

3.2 Crack branching under high strain rates

This example deals with the crack branching in a linear elastic porous media. Figure 8 plots the dimensions of the specimen with an initial crack and the loading conditions. The stress applied on the top and bottom boundaries is defined as

$$\sigma_{y} = \begin{cases} \frac{\sigma_{y_{max}}t}{t_{0}} & \text{if } t < t_{0} \\ \sigma_{y_{max}} & \text{if } t \ge t_{0} \end{cases}$$
(37)

where $t_0=6.25~\mu s$ and $\sigma_{y_{max}}=8$ MPa. A stable time step $\Delta t=0.025~\mu s$ is chosen. The specimen is discretized into 200×80 material points with a uniform grid ($\Delta x=0.5$ mm). The horizon $\delta=4.05\Delta x$. The material parameters for this example are density $\rho^s=2650$ kg/m 3 , initial volume fraction $\phi_0=0.95$, $\lambda=14\times10^3$ MPa, $\mu=14\times10^3$ MPa, $\mu_c=\mu/3$, $\alpha_3=56\times10^3$ kN, $\alpha_1=\alpha_2=0$, the micro-polar length scale l=2 mm, and the critical energy release rate $G^{cr}=160$ N/m for the energy-based bond breakage criterion.

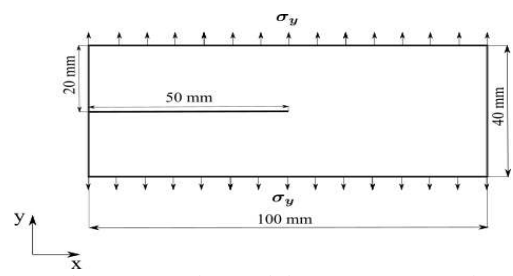


Figure 8. Schematic of the model setup for example 2

Figure 9 plots the loading curve versus the time on which four points are chosen to present the following results. Figure 10 plots the crack growth and branching on the deformed configuration. The crack path in Figure 10 is in red (damaged variable greater than 0.35). The results show that the crack grows at point 1, and the branching begins at point 2.

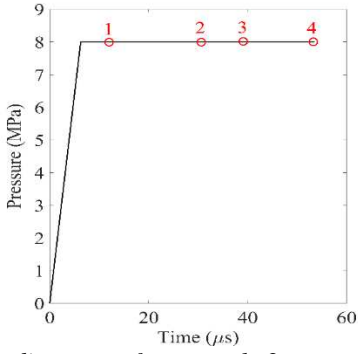
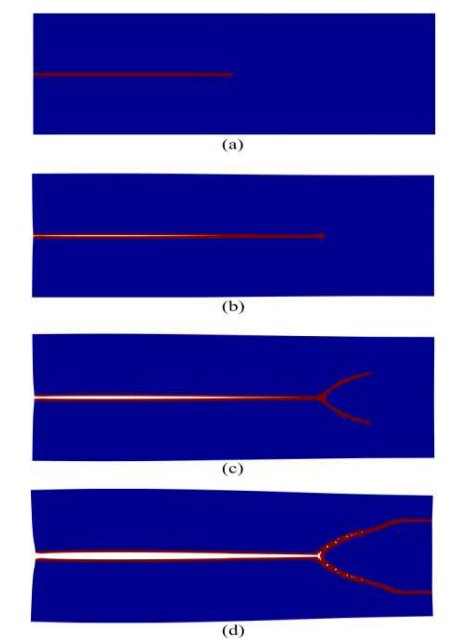


Figure 9. Loading curve for example 2



Figures 10. Crack growth and branching at t = (a) 12.75 μ s, (b) 29.75 μ s, (c) 42.5 μ s, and (d) 55.5 μ s

Next, we present the simulations with three loading rates to demonstrate the loading rate effect on crack growth and branching. The different loading rates are realized by assuming $t_0 = 2.5 \mu s$, 6.25 μs , and 12.5 μs ,

respectively. The material parameters remain the same, except that $\phi_0=0.85$. Table 1 summarizes the timing of the crack growth and branching. The results show that decreasing the loading rate delays the timing of crack growth and branching. Figure 11 plots the contours of the damage variable at $t=45~\mu s$. Figure 12 plots the contours of the micro rotation at $t=37.5~\mu s$. The results show that loading rates can significantly affect crack branching and micro-rotation.

Table 1. Summary of the timing of cracking process

$t_0(\mu s)$	Start(µs)	Branching(μs)	End (μs)
2.5	7.5	23.75	47.5
6.25	9.75	25.5	50
12.5	12.75	28.75	52.5

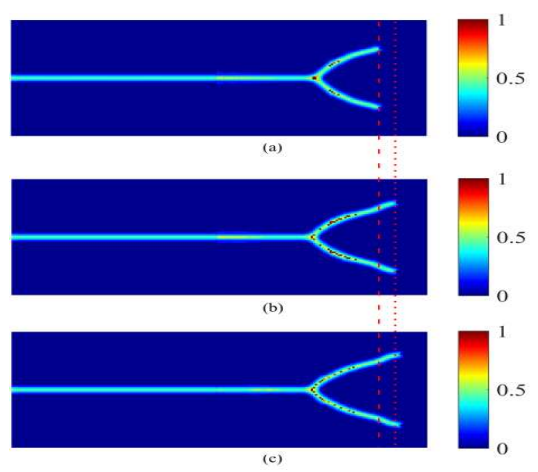


Figure 12. Contours of the damage variable at $t=45~\mu s$ from the simulations: (a) $t_{0,1}=12.5~\mu s$, (b) $t_{0,2}=6.25~\mu s$, and (c) $t_{0,3}=2.5~\mu s$

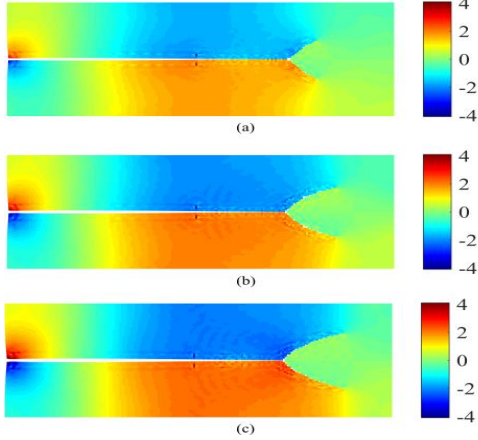


Figure 13. Contours of the micro rotation (0.001 rad) at $t=37.5~\mu s$ from the simulations: (a) $t_{0,1}=12.5~\mu s$, (b) $t_{0,2}=6.25~\mu s$, and (c) $t_{0,3}=2.5~\mu s$

4 CONCLUSIONS

We have reformulated the periporomechanics through the Cosserat continuum for modeling shear banding and crack branching in porous media. The governing equations consist of the balance equations of linear momentum and moment. The Cosserat constitutive correspondence principle is used to incorporate the classical micro-polar elastoplastic constitutive model into the proposed framework. The damage and cracking are modeled through an energy-based bond breakage criterion. Numerical examples are presented to show the robustness of the Cosserat periporomechanics paradigm for modeling shear banding and crack branching in porous media under dynamic loads (e.g., high loading rates).

5 ACKNOWLEDGEMENTS

This work was supported by the US National Science Foundation under contract number 1944009. The authors thank the two anonymous reviewers for their constructive review of the original version of this article.

6 REFERENCES

Menon, S., Song, X. 2021a. A stable computational nonlocal poromechanics model for dynamics analysis of saturated porous media, *International Journal for Numerical Methods in Engineering* **122**, 5512–5539.

Menon, S., Song, X. 2021b. A computational periporomechanics model for localized failure in unsaturated porous media. Computer Methods in Applied Mechanics and Engineering, 384, p.113932.

Menon, S., Song, X. 2022a. Computational multiphase periporomechanics for un-guided cracking in unsaturated porous media, *International Journal for Numerical Methods* in Engineering 123, 2837–2871.

Menon, S., Song, X., 2022b. Updated Lagrangian unsaturated periporomechanics for extreme large deformation in unsaturated porous media. *Computer Methods in Applied Mechanics and Engineering*, 400, p.115511.

Menon, S., Song, X. 2023. Computational coupled large deformation periporomechanics for dynamic failure and fracturing in variably saturated porous media. International *Journal for Numerical Methods in Engineering*, 124(1), 80-118.

Silling, S. A., Epton, M., Weckner, O., Xu, J., Askari, E. 2007. Peridynamic States and Constitutive Modeling, *Journal of Elasticity* **88**, 151–184.

Song, X., Borja, R. I. 2014. Mathematical framework for unsaturated flow in the finite deformation range, *International Journal for Numerical Methods in Engineering* **97**, 658–682.

Song, X., Ye, M. and Wang, K., 2017. Strain localization in a solid-water-air system with random heterogeneity via stabilized mixed finite elements. *International Journal for Numerical Methods in Engineering*, 112(13), 1926-1950.

Song, X., Silling, S. A. 2020. On the peridynamic effective force state and multiphase constitutive correspondence principle, *Journal of the Mechanics and Physics of Solids* **145**, 104–161.

Sulem, J. Vardoulakis I. 1995. *Bifurcation analysis in geome-chanics*, CRC Press.